Experimental Mechanics (2011) 51:1155–1169
DOI 10.1007/s11340-010-9410-y

Simultaneous Measurement of Effective Chemical Shrinkage and Modulus Evolutions During Polymerization

Y. Wang · L. Woodworth · B. Han

Received: 18 May 2010 / Accepted: 6 September 2010 / Published online: 1 October 2010
© Society for Experimental Mechanics 2010

Abstract A novel method is proposed to *simultaneously* measure the effective chemical shrinkage and modulus evolutions of advanced polymers during polymerization. The method utilizes glass fiber Bragg grating (FBG) sensors. They are embedded in two uncured cylindrical polymer specimens with different configurations and the Bragg wavelength (BW) shifts are continuously documented during the polymerization process. A theoretical relationship is derived between the BW shifts and the evolution properties, and an inverse numerical procedure to determine the properties from the BW shifts is established. Extensive numerical analyses are conducted to provide general guidelines for selecting an optimum combination of the two specimen configurations. The method is implemented for a high-temperature curing thermosetting polymer. Validity of the proposed method is corroborated by two independent verification experiments: a self-consistency test to verify the measurement accuracy of raw data and a warpage measurement test of a bi-material strip to verify the accuracy of evolution properties.

Keywords Effective chemical shrinkage · Elastic modulus · Evolution · Fiber Bragg grating · Gelation point

Introduction

Thermosetting polymers are widely used in the semiconductor industry. During polymerization, they undergo significant reduction of volumes as molecules move from a van der Waals distance of separation to a covalent distance of separation. This volumetric shrinkage induced by the polymerization is called "*chemical shrinkage*." The chemical shrinkage produces dimensional changes and residual stresses in packaged devices, which can significantly affect product reliability [1–3]. In some cases, the chemical shrinkage affects the functionality of special polymers. For example, electrically conductive adhesives with higher curing shrinkage generally exhibit higher conductivity [4]. Measuring the chemical shrinkage of base polymers is critically needed for performance optimization.

Numerous methods have been developed in the past few decades [5–11] to measure the *intrinsic (or total) chemical shrinkage* (denoted as ε_k) both during [7–9, 11] and at the end of the polymerization process [5, 6, 10]. It is important to note that not all of the intrinsic chemical shrinkage contributes to the dimensional stability or the residual stress, since some portion of the chemical shrinkage occurs before the gelation point where polymers start to build mechanical strength [12–14]. The chemical shrinkage after the gelation point, called the "*effective chemical shrinkage*" (denoted as ε^{ch}) [15], should be used for calculation of curing-induced deformations; otherwise, the magnitude of deformations can be significantly overestimated. The existing methods measure the intrinsic chemical shrinkage simply because they cannot detect the gelation point. Additional techniques such as the Rheometrics Dynamic Spectrometer [16] can be used together with the existing methods to measure the effective chemical shrinkage. However, this additional technique greatly increases the complexity of the experimental procedure and does not seem practical for routine practice.

Another important property that is required for accurate determination of the residual deformations is *Young's modulus*. During the dynamic curing process of polymers, the Young's modulus evolves non-linearly with the time as polymerization proceeds. To the best of the authors' knowledge, a rheometer

Y. Wang · L. Woodworth · B. Han (✉, SEM Fellow)
Department of Mechanical Engineering, University of Maryland, College Park, MD 20742, USA
e-mail: bthan@umd.edu

or a Dynamic Mechanical Analyzer (DMA) is the only available technique that can measure the modulus evolution during polymerization [17–19].

An increment of chemical shrinkage, $d\varepsilon_k$, contributes to the residual deformation during polymerization [18]. In the case of uni-axial loading, the increment of the residual stress, $d\sigma_R$, can be expressed as

$$d\sigma_R = Ed\varepsilon_k \tag{1}$$

By integrating equation (1) over the entire curing process, the residual stress, σ_R, can be estimated as

$$\sigma_R = \int Ed\varepsilon_k = \int_0^{t_{gel}} (E(t)\cdot\dot{\varepsilon}_k(t))dt + \int_{t_{gel}}^{t_{final}} (E(t)\cdot\dot{\varepsilon}_k(t))dt = \int_{t_{gel}}^{t_{final}} \left(E(t)\cdot\dot{\varepsilon}^{ch}(t)\right)dt \tag{2}$$

where t_{gel} and t_{final} are the times of gelation point and of complete polymerization, respectively.

The evolution of the effective chemical shrinkage, $\varepsilon^{ch}(t)$, and the evolution of the modulus, $E(t)$, can be measured by two different techniques. It is important to note, however, that the correct time correlation and identical curing conditions are extremely difficult to achieve in practice when different techniques are employed to measure each quantity separately.

Many researchers have attempted to characterize the evolution of curing-induced residual stresses of bi-material strips [20, 21] by measuring the bending deformation during polymerization. However, the measured results pertain to specimens with the specific dimensions and configurations used in their experiments, and the experimental results cannot be extended to the complex configurations of packaged assemblies.

We propose a novel method to cope with the technical difficulties associated with the existing techniques. It utilizes fiber Bragg grating (FBG) sensors to simultaneously measure the effective chemical shrinkage and modulus evolutions. The basic concept of polymer property measurements using FBG sensors has been reported in Ref. [15]. In this study, the concept is advanced for measurement of the property evolutions during the entire polymerization process.

In our previous study, only the final chemical shrinkage in the complete polymerization state was of interest and it was decoupled from the modulus by employing a large specimen configuration. The large configuration reduced the mathematical complexity substantially and thus simplified the numerical procedure. For the current study of interest, namely evolutions during polymerization, however, the large configuration is applicable only to polymers that have extremely long curing time (or very small heat generation), as otherwise the measurement accuracy can be affected significantly by a temperature overshooting and a temperature gradient within a specimen. In this paper, the issue is addressed and a more general method is developed.

The concept of the proposed method is first described. A numerical procedure to determine the property evolutions from the BW shifts is followed. The rationale to determine a proper set of specimen configurations is described and demonstrated for different polymers. The proposed method is implemented with an underfill material. The evolutions of effective chemical shrinkage and modulus are measured and the results are validated by direct measurement data.

Mathematical Formulations

Elastic Solution of an FBG Embedded in Cylindrical Substrate

The proposed method utilizes the basic characteristic of the FBG, which is embedded in a polymer. As illustrated in Fig. 1, a polymer of interest is cured around an FBG. Consider a small time increment during polymerization. A shrinkage strain of $\Delta\varepsilon^{ch}$ occurs in the polymer substrate over the time increment, which has an instant modulus of E_s. The loading condition of the incremental time duration can be written mathematically as

$$\varepsilon(z) = \begin{cases} 0 & \text{for } 0 \le r < a \\ \Delta\varepsilon^{ch} & \text{for } a < r \le b \end{cases} \tag{3}$$

where a is the radius of the FBG and b is the radius of the polymer substrate. From the theory of elasticity, the generalized plane strain solution of stress components within the fiber can be derived as:

$$\sigma_{rr}^f = \sigma_{\theta\theta}^f = \frac{E_f}{1+\nu_f}\cdot\frac{C_{1f}}{1-2\nu_f} \tag{4}$$

$$\sigma_{zz}^f = \frac{2\nu_f E_f C_{1f}}{(1+\nu_f)(1-2\nu_f)} + \frac{\left(\frac{b^2}{a^2}-1\right)\left[\frac{E_s}{1-\nu_s}\Delta\varepsilon^{ch} - \frac{2\nu_s E_s C_{1s}}{(1+\nu_s)(1-2\nu_s)}\right] - \frac{2\nu_f E_f C_{1f}}{(1+\nu_f)(1-2\nu_f)}}{1+\frac{E_s}{E_f}\left(\frac{b^2}{a^2}-1\right)} \tag{5}$$

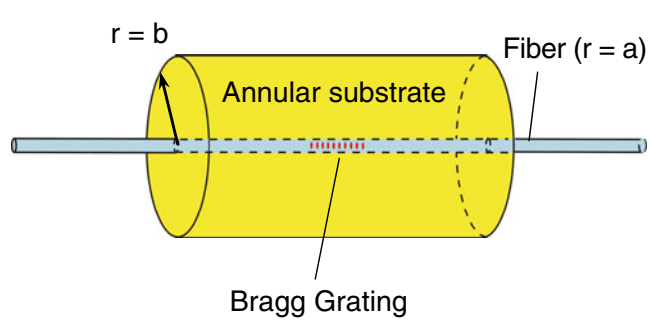

Fig. 1 Schematic diagram of an FBG sensor embedded in a cylindrical substrate

where σ^f_{zz}, σ^f_{rr} and $\sigma^f_{\theta\theta}$ are the axial, radial and hoop stress components of the FBG, respectively; E_f and v_f are the modulus and the Poisson's ratio of the fiber material; and E_s and v_s are the modulus and the Poisson's ratio of the polymer. The details of the derivation can be found in Ref. [15]. The coefficients, C_{1f} and C_{1s} in equations (4) and (5), have the form of

$$C_{1f} = \frac{A+B}{C+D}\left(1-\frac{b^2}{a^2}\right)\frac{E_s}{E_f}\frac{(1+v_f)(1-2v_f)}{(1+v_s)(1-2v_s)} + \frac{E_s}{E_f} \times \left(\frac{b^2}{a^2}-1\right)\frac{(1+v_f)(1-2v_f)}{1-v_s}\frac{\Delta\varepsilon^{ch}}{2} \tag{6}$$

$$C_{1s} = \frac{A+B}{C+D} \tag{7}$$

where A, B, C and D are coefficients and they can be expressed as

$$A = \left(\frac{b^2}{a^2}-1\right)\frac{\Delta\varepsilon^{ch}}{1-v_s}\left[\frac{1+v_s}{2} - \frac{(v_f-v_s)\frac{E_s}{E_f}}{1+\frac{E_s}{E_f}\left(\frac{b^2}{a^2}-1\right)}\right] \tag{8}$$

$$B = \frac{E_s}{E_f}\left(\frac{b^2}{a^2}-1\right)\frac{\Delta\varepsilon^{ch}}{2}\frac{(1+v_f)(1-2v_f)}{(1-v_s)} \times \left\{1+\frac{2v_f(v_f-v_s)}{(1+v_f)(1-2v_f)\left[1+\frac{E_s}{E_f}\left(\frac{b^2}{a^2}-1\right)\right]}\right\} \tag{9}$$

$$C = 1+\frac{b^2}{a^2}\frac{1}{1-2v_s} - \frac{E_s}{E_f} \times \frac{2v_s(v_f-v_s)\left(\frac{b^2}{a^2}-1\right)}{(1+v_s)(1-2v_s)\left[1+\frac{E_s}{E_f}\left(\frac{b^2}{a^2}-1\right)\right]} \tag{10}$$

$$D = \frac{E_s}{E_f}\left(\frac{b^2}{a^2}-1\right)\frac{(1+v_f)(1-2v_f)}{(1+v_s)(1-2v_s)} \times \left\{1+\frac{2v_f(v_f-v_s)}{(1+v_f)(1-2v_f)\left[1+\frac{E_s}{E_f}\left(\frac{b^2}{a^2}-1\right)\right]}\right\} \tag{11}$$

Equations (3) to (11) complete the mechanical description of the stress states of the FBG when the polymer matrix undergoes a chemical shrinkage of $\Delta\varepsilon^{ch}$.

Bragg Wavelength Shift and Evolution Properties

The Bragg wavelength (BW) will shift as the temperature or strain state of the FBG changes. Theoretically, the total BW shift can be expressed as [15]

$$\Delta\lambda_B = \Delta\lambda^i_B + \Delta\lambda^d_B \tag{12}$$

The first term, $\Delta\lambda^i_B$, is called the "*intrinsic*" BW shift, which is not associated with any stress-induced deformation. It is defined as

$$\Delta\lambda^i_B = \lambda_B\left(\alpha_f + \frac{1}{n_{eff}}\frac{dn}{dT}\right)\Delta T \tag{13}$$

where λ_B is the initial Bragg wavelength (BW), α_f is the CTE of the fiber core material, n_{eff} is the effective refractive index, $\frac{dn}{dT}$ is the thermo-optic constant, and ΔT is the temperature change with respect to a initial condition.

The second term, $\Delta\lambda^d_B$, is called the "*deformation*" induced BW shift. It has been shown in equation (4) that the FBG is subjected to a uniform transverse loading condition, i.e., the radial stress equals to the hoop stress while embedded in a cylindrical substrate. Then the "*deformation*" induced BW shift can be formulated in terms of stress components as [15]

$$\Delta\lambda^d_B = \frac{\lambda_B}{E_f}\left\{\begin{array}{l}\left[1-\frac{n^2_{eff}}{2}\left(P_{12}-(P_{12}+P_{11})\upsilon_f\right)\right]\sigma^f_{zz} - \\ \left[2\upsilon_f+\frac{n^2_{eff}}{2}\left((1-\upsilon_f)P_{11}+(1-3\upsilon_f)P_{12}\right)\right]\sigma^f_{rr}\end{array}\right\} \tag{14}$$

where P_{11} and P_{12} are strain-optic coefficients (Prockel's coefficients).

After substituting equation (4) and (5) into equation (14), the BW shift produced by a chemical shrinkage of $\Delta\varepsilon^{ch}$ can be formulated. The governing equation will take a form of

$$\Delta\lambda^d_B = F(E_s,\beta)\cdot\Delta\varepsilon^{ch} \tag{15}$$

where $\beta = \frac{b}{a}$. The nonlinear function, F, is written as

$$F(E_s,\beta) = \frac{G_1(\beta)(E_s/E_f) + G_2(\beta)(E_s/E_f)^2}{2\cdot\left[H_0(\beta)+H_1(\beta)(E_s/E_f)+H_2(\beta)(E_s/E_f)^2\right]}(\beta^2-1)\lambda_B \tag{16}$$

where G_1, G_2, H_0, H_1 and H_2 are functions of β and they can be expressed as

$$G_1(\beta) = (1+\nu_s)\begin{bmatrix} 2\beta^2 + 2 - 4\nu_f + n_{eff}^2 P_{11}\left(\nu_f\beta^2 + 2\nu_f - 1\right) \\ - n_{eff}^2 P_{12}\left(\left(1-\nu_f\right)\beta^2 + 2 - 4\nu_f\right) \end{bmatrix} \tag{17}$$

$$G_2(\beta) = \left(1 - \nu_f - 2\nu_f^2\right)\left(2 - 2n_{eff}^2 P_{12} - n_{eff}^2 P_{11}\right)\left(\beta^2 - 1\right) \tag{18}$$

$$H_0(\beta) = (1+\nu_s)\left(\beta^2 + 1 - 2\nu_s\right) \tag{19}$$

$$H_1(\beta) = \left(\beta^2 - 1\right)\left(\nu_s\beta^2 + \beta^2 + 2 - 4\nu_f\nu_s - \nu_s - \nu_f\right) \tag{20}$$

$$H_2(\beta) = \left(1 - \nu_f - 2\nu_f^2\right)\left(\beta^2 - 1\right)^2 \tag{21}$$

Since there are only two unknown constants (effective chemical shrinkage and modulus) in the governing equation, they can be inversely determined from the BW shifts measured from two configurations with different values of β; they will be referred to as C-1 and C-2, respectively, which correspond to β_1 and β_2 ($\beta_1 > \beta_2$).

The BW shift of two configurations can be written as

$$\begin{cases} \Delta\lambda_B^{C-1} = F(E_s, \beta_1)\cdot\Delta\varepsilon^{ch} \\ \Delta\lambda_B^{C-2} = F(E_s, \beta_2)\cdot\Delta\varepsilon^{ch} \end{cases} \tag{22}$$

where $\Delta\lambda_B^{C-1}$ and $\Delta\lambda_B^{C-2}$ are the deformation induced BW shifts of C-1 and C-2, respectively. The superscript, d, of the deformation induced BW shift will hereafter be omitted for convenience. Dividing equation (22) side by side yields

$$\frac{\Delta\lambda_B^{C-1}}{\Delta\lambda_B^{C-2}} = \frac{F(E_s, \beta_1)}{F(E_s, \beta_2)} \tag{23}$$

The ratio of the BW shifts is independent of the chemical shrinkage increment, which allows the following sequential procedure to determine the evolution properties as a function of time.

Calculation of Evolution Properties

The suggested procedure to calculate the evaluation properties is illustrated in Fig. 2, where the BW shifts of the two configurations are illustrated. It is to be noted

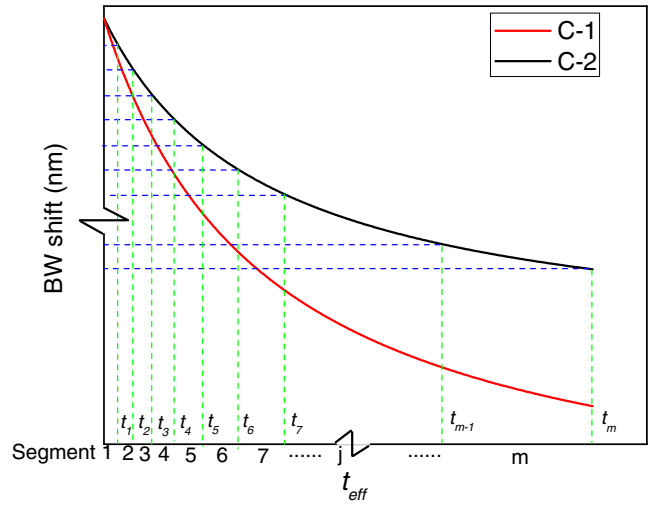

Fig. 2 BW shifts after the gelatin point and the segment division

that the horizontal axis represents time after the gelation point. The BW shift will not occur (or be negligible if any) before the gelation point; the effective time after the gelation point (t_{eff}) is defined as $t_{eff} = t - t_{gel}$.

When the curing is completed, the magnitude of $\Delta\lambda_B^{C-1}$ is larger than that in $\Delta\lambda_B^{C-2}$, as expected from the larger volume rigidity of C-1. For this reason, the BW shifts of C-2 are first divided into m small constant segments. For the jth (j=1 to m) time segment $\left(t_{j-1} < t_{eff} < t_j\right)$, we define

$\Delta\lambda_{B,j}^{C-1}$ and $\Delta\lambda_{B,j}^{C-2}$: BW shift increments of configuration C-1 and C-2
$E_{s,j}$: Instant equilibrium modulus (averaged over the time segment)
$\Delta\varepsilon_j^{ch}$: Chemical shrinkage increment

Then equations (22) and (23) can be written for the jth segment as

$$\begin{cases} \Delta\lambda_{B,j}^{C-1} = F\left(E_{s,j}, \beta_1\right)\cdot\Delta\varepsilon_j^{ch} \\ \Delta\lambda_{B,j}^{C-2} = F\left(E_{s,j}, \beta_2\right)\cdot\Delta\varepsilon_j^{ch} \end{cases} \tag{24}$$

$$\frac{\Delta\lambda_{B,j}^{C-1}}{\Delta\lambda_{B,j}^{C-2}} = \frac{F\left(E_{s,j}, \beta_1\right)}{F\left(E_{s,j}, \beta_2\right)} \tag{25}$$

The average modulus over this segment, $E_{s,j}$, can be determined using equation (25). Then, by substituting $E_{s,j}$ back into either one of equation (24), $\Delta\varepsilon_j^{ch}$ can be calculated. By repeating the above calculations, the shrinkage increment and the instant equilibrium modulus in every

segment can be determined. The property evolutions can then be expressed as

$$\varepsilon^{ch}(t_j) = \sum_{i=1}^{j} \Delta\varepsilon_i^{ch} \quad (\text{for } j = 1 \text{ to } m) \qquad (26)$$
$$E_s(t_j) = E_{s,j}$$

At a given instant, t_{eff}, the modulus is defined as an instantaneous value while the chemical shrinkage is defined as a value accumulated up to that instant.

To enhance the accuracy in solving equation (25), it is desired to make the BW shift ratios $\left(\frac{\Delta\lambda_B^{C-1}}{\Delta\lambda_B^{C-2}}\right)$ as large as possible, which can be achieved by increasing the ratio of the two configurations $(M = \beta_1/\beta_2)$.

Optimum Specimen Configurations

The ratio can be increased by using either a large value of β_1 or a small value of β_2. In practice, the lower bound of the smaller configuration C-2 is limited by the resolution of a measurement system, while the upper bound of the larger configuration C-1 is limited by excessive heat produced by the exothermic polymerization process. The following numerical analysis is conducted to provide a guideline for selecting the optimum specimen configurations.

C-2 Configuration

The lower bound of the C-2 configuration is limited by the sensitivity of BW measurement system because smaller specimen configurations produce proportionally small deformations of the polymer/FBG assembly and thus reduce the signal of the FBG. The criterion acceptable for the 95% engineering accuracy can be written as

$$\Delta\lambda_{B,j}^{C-2} = F(E_{s,j}, \beta_2) \cdot \Delta\varepsilon_j^{ch} > 20\delta_{\lambda_B} \qquad (27)$$

where δ_{λ_B} is the BW measurement resolution. Considering a minimum of ten segments (ten data points) to describe the nonlinear nature of two property evolutions faithfully, the required minimum BW shift for each segment should be at least 20 pm (or a total of 200 pm) given the fact that a typical fiber Bragg grating interrogating system provides a measurement resolution of ≈1 pm.

A simple material system following an nth order model [17, 22–27] is considered to illustrate the above criterion quantitatively. The model can be expressed as

$$\frac{dp}{dt} = k_c(1-p)^n \qquad (28)$$

where p is the curing extent and k_c is a temperature-dependent rate coefficient. The rate coefficient is related to the temperature through Arrhenius's equation

$$k_c = Ae^{-\frac{E_a}{RT}} \qquad (29)$$

where A is a material constant, E_a is the activation energy and R is the ideal gas constant (8.314*J/mol·K*).

The relation between the effective chemical shrinkage and the curing extent can be modeled as

$$\varepsilon^{ch}(t_{eff}) = \varepsilon_\infty^{ch} \cdot \phi(p) \qquad (30)$$

where ε_∞^{ch} is the effective chemical shrinkage after the complete curing. Theoretically the function, $\phi(p)$, can take any mathematical form of p; e.g., a linear function of $\phi(p)$ has been reported for various polymer systems [28, 29].

The relation between the modulus and the curing extent can be modeled as

$$E(t) = E_\infty(T) \cdot \phi(p) \qquad (31)$$

where E_∞ is a temperature-dependent equilibrium modulus when the polymer is fully cured. The function, $\phi(p)$, can also take any mathematical form of p. The percolation theory [30, 31] is adopted in this study, which can be expressed as

$$E(t) = \begin{cases} 0 & \text{if } p < p\,gel \\ E_\infty\left(\frac{p^2-p_{gel}^2}{1-p_{gel}^2}\right)^{8/3} & \text{if } p \geq p\,gel \end{cases} \qquad (32)$$

where p_{gel} is the curing extent at the gelation point; a typical value of p_{gel} is around 0.5 [14, 32–35].

The most representative values of thermosetting polymers were used in the simulation. The curing kinetics parameters were A=29.1/s, E_a=35.8*kJ/mol*, n=2 with a curing temperature of 165°C [17]. They yield a polymerization rate of $k_c \approx 0.002/s$ at the curing temperature [17, 22–27]. Polymers develop a small modulus at the end of the curing, especially when they are cured at elevated temperatures. Depending on the material, E_∞ can vary from hundreds of MPa to several GPa. A value of 100 MPa was chosen for the calculation, which was the low end of reported moduli [18, 20, 30, 36–40]. For the total chemical shrinkage, a representative value of 0.9% was chosen based on the literature [5–8, 11, 41–47]. Assuming the linear function of $\phi(p)$ and p_{gel}=0.5, the corresponding effective chemical shrinkage at the gelation point was 0.45%.

In the calculation procedure, the whole curing process was first divided into m small uniform segments with the time increment of Δt. The time at the beginning and the end of the jth (j=1 to m) segment are $(j-1)\Delta t$ and $j\Delta t$, respectively. The curing extent at the beginning and the end of the jth (j=1 to m) segment was determined from equation (28). Then, the chemical shrinkage increment and the

average equilibrium modulus of the jth segment were determined from equations (30) and (32). The evolution properties of this material system are plotted in Fig. 3(a). The figure also shows the effective chemical shrinkage and the effective time defined earlier.

For the material system plotted in Fig. 3(a), the simulated BW shift evolution of configuration β=20 is plotted in Fig. 3(b). Typical properties of glass FBGs were used in the simulation: P_{11}=0.121, P_{12}=0.270 [48–50], E_f= 73.1 GPa [51], ν_f=0.17 [49, 52] and n_{eff}=1.457 [53]. The BW evolves non-linearly with the time. A total BW shift of 0.522 nm is observed at the end of the curing process.

To better understand the effect of the configuration on the signal amplitude, the total BW shifts for various configurations (β) are plotted in Fig. 4, where a dashed line indicates the criterion of equation (27). In Fig. 4, two different cases of the total chemical shrinkage ε_k=0.45% and 0.90% are plotted. As expected, the BW shift decreases considerably as the chemical shrinkage decreases. The analysis indicates that, for typical polymers, the configuration of β_2 larger than 17 will produce a BW signal, which is sufficiently large for accurately determination of properties. It is important to note that the amount of BW shift is function of only the radius ratio (b/a). Therefore, the above analysis will be valid for any FBGs. In the following calculation, β_2 of 20 is used as C-2 for simplicity.

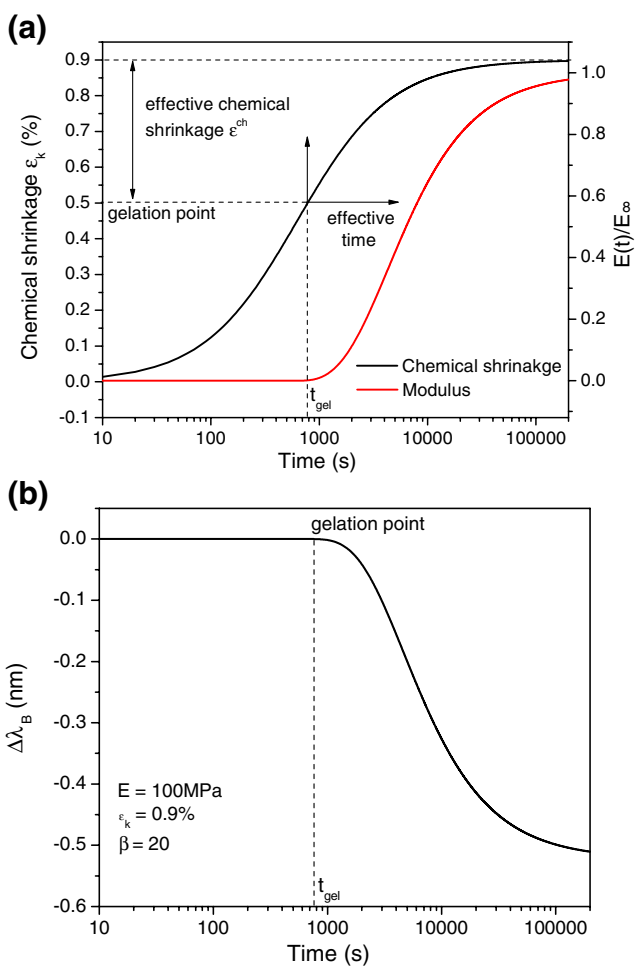

Fig. 3 Illustration of (**a**) chemical shrinkage and modulus evolutions and (**b**) BW shift evolution of configuration β=20

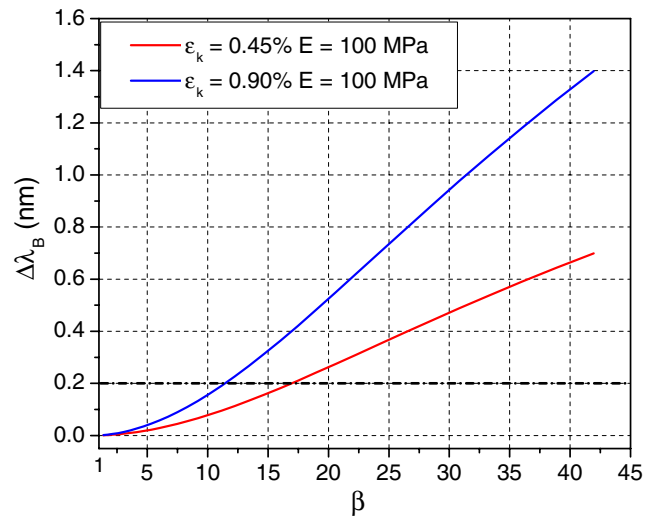

Fig. 4 Simulated BW shifts of different specimen configurations

C-1 Configuration

As mentioned earlier, it is desired to make the ratio of the two configurations ($M = \beta_1/\beta_2$) as large as possible for the accuracy of the inverse calculations. Figure 5 illustrates the fact quantitatively. The plot of Fig. 5 shows the BW shift ratios $\left(\frac{\Delta\lambda_B^{C-1}}{\Delta\lambda_B^{C-2}}\right)$ for the given C-2 configuration (β_2=20) as a function of various C-1 configurations (β_1), where the

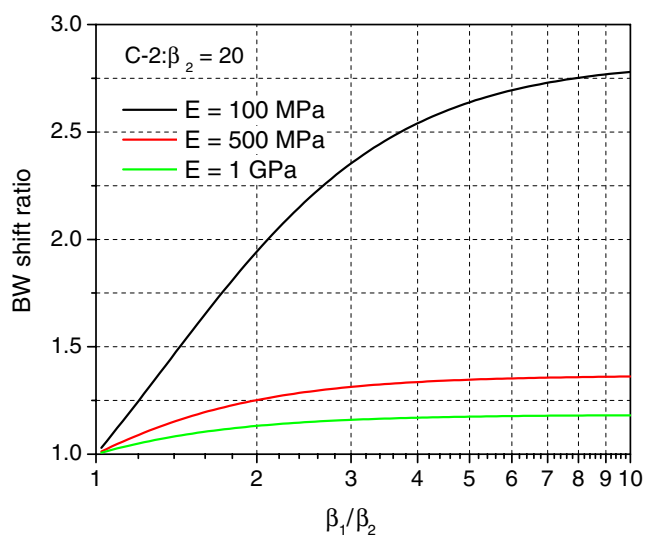

Fig. 5 BW shift ratio of various C-1 configurations

BW shift ratios are shown for three different elastic moduli (100 MPa, 500 MPa and 1 GPa). It clearly shows that the BW shift ratio and thus the measurement accuracy increases as C-1 configuration becomes larger. The practical upper value of β_1 is limited by the effect of heat generated during polymerization (exothermic process) on BG shift measurements. A combined numerical analysis of curing kinetics and heat generation is conducted to provide a guideline to select a proper C-1 configuration.

For a polymer with a cylindrical shape, the Fourier's heat conduction equation has the form of

$$k\left(\frac{\partial^2 T}{\partial r^2}+\frac{1}{r}\frac{\partial T}{\partial r}\right)+\dot{q}=\rho c_p\frac{\partial T}{\partial t} \tag{33}$$

where k is the thermal conductivity, T is the temperature, t is the time, ρ is the density, c_p is the specific heat and $\dot{q}$ is the heat generation rate, which is directly related to the reaction speed through the equation

$$\dot{q}=\rho\Delta H\frac{dp}{dt} \tag{34}$$

where p is the curing extent and ΔH is the total exotherm of the reaction. An nth order curing kinetics model in equation (28) is used in the following analysis for its mathematic simplicity, but any other complicated explicit models can also be used.

Substituting equations (28), (29) and (34) into equation (33) will yield the governing equations for thermal modeling of polymerization process as

$$\frac{k}{\rho}\left(\frac{\partial^2 T}{\partial r^2}+\frac{1}{r}\frac{\partial T}{\partial r}\right)+Ae^{-\frac{E_a}{RT}}(1-p)^n\Delta H=c_p\frac{\partial T}{\partial t} \tag{35}$$

where

$$\frac{dp}{dt}=Ae^{-\frac{E_a}{RT}}(1-p)^n \tag{36}$$

The boundary conditions are

$$\begin{cases} T|_{t=0}=T_0 \\ -k\frac{\partial T}{\partial r}\Big|_{r=b}=h(T-T_a) \\ p|_{t=0}=0 \end{cases} \tag{37}$$

where h is the convective heat transfer coefficient and T_a is the ambient temperature and T_0 is the initial temperature. Equation (35) is highly nonlinear but can be solved using the finite element method.

The area of the polymer is first discretized into a total of N nodes. The whole polymerization process is divided into l steps with a small time interval of Δt. The temperature distribution of the first time step is calculated through a transient analysis with a uniform heat generation. The resultant non-uniform temperature distribution is used to determine the curing extent of the second time step at each node using equation (36): in the ith (from 2 to l) time step, the curing extent at node j (from 1 to N) can be approximated as

$$p_{i,j}=Ae^{-\frac{E_a}{RT_{i-1,j}}}(1-p_{i-1,j})^n\Delta t+p_{i-1,j} \tag{38}$$

where $T_{i\text{-}1,j}$ is the temperature at node j in the i-1th (from 1 to l−1) time step. The heat generation rate of each node is then updated according to equation (34). Using the updated curing extent and heat generation rate at each node, the temperature distribution is calculated for the next time step. The procedure is iterated until all time steps are completed. The evolutions of the curing extent and the temperature distribution are obtained by recording the intermediate results during the polymerization process.

The maximum temperature and thus maximum curing extent difference will occur between the center of C-1 and the surface of C-2. This maximum curing extent difference, Δp_{max} can be used as a metric to select a proper C-1 configuration. For the predetermined C-2 configuration (β_2=20), Δp_{max} of various C-1 configurations were calculated using the numerical analysis used in the previous section.

A wide range of the total exotherm and the rate coefficient was considered: ΔH from 200 to 400J/g and k_c from $0.8\cdot10^{-3}$ to $3.2\cdot10^{-3}/s$. This range covers most of the thermosetting polymers used in semiconductor packaging applications. The simulation results are shown in Fig. 6, where Δp_{max} for three discrete total exotherm values of 200, 300 and 400J/g are plotted as a function of C-1 configuration (β_1) in (a), (b) and (c), respectively. Each plot contains Δp_{max} distributions for three rate coefficient values of $0.8\cdot10^{-3}/s$, $1.6\cdot10^{-3}/s$ and $3.2\cdot10^{-3}/s$.

When Δp_{max} is less than 1%, it is reasonable to assume that polymer in the two configurations cure uniformly (within the configurations) and consistently (between the two configurations). This guideline is also illustrated in Fig. 6.

In practice, the curing kinetics of the material can be first measured by a differential scanning calorimeter (DSC) and a proper C-1 specimen configuration can be determined using Fig. 6. For example, if a polymer has a small exotherm (≈200J/g) [Fig. 6(a)], β=40 can be used for C-1 configuration even when it cures at a high rate of $3.2\cdot10/s$. For typical polymers used in the previous analysis (k_c= $2\cdot10^{-3}/s$ and 300J/g), $\beta\approx50$ can be used for C-1 configuration [Fig. 6(b)]. For those polymers with a higher total exotherm, the value of β has to be proportionally reduced for C-1 configuration [Fig. 6(c)].

Implementation

The proposed method was implemented with a high temperature curing underfill material. After the description

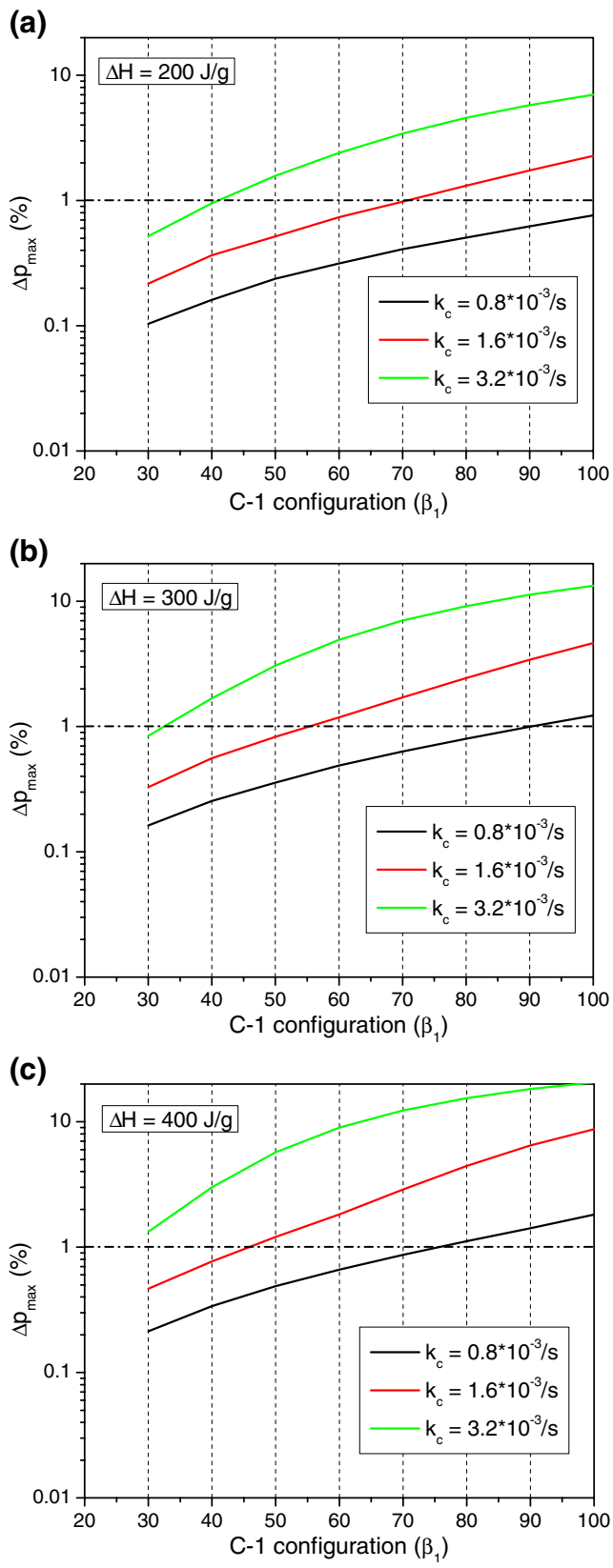

Fig. 6 Δp_{max} of various C-1 configurations (**a**) ΔH=200*J/g*; (**b**) ΔH=300 *J/g*; (**c**) ΔH=400*J/g*

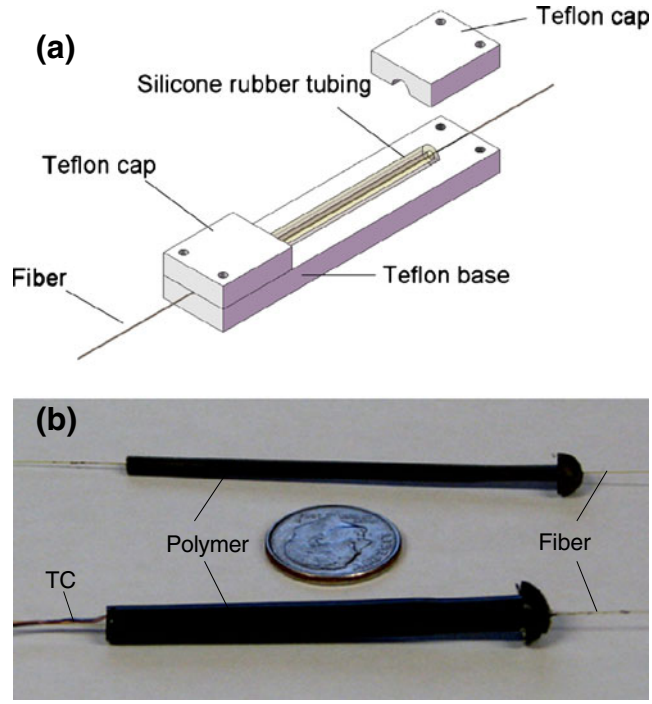

Fig. 7 (**a**) Mold assembly to fabricate polymer specimens and (**b**) C-1 and C-2 configurations of underfill material fabricated by the mold assembly

of a mold to fabricate the specimen is given, a supplementary work using DSC is reported, which guides to determine C-1 configuration (Fig. 6). The evolution property measurements using the selected configurations are reported.

Experimental Setup

The mold assembly to fabricate the specimen is shown in Fig. 7(a). The mold consists of a base, two caps and a silicone rubber tube. The base and two caps were made of Teflon. Teflon can resist high temperature and do not adhere to polymers. Very fine grooves were fabricated along the centerline in the base mold to hold an FBG. The polymer was cured in a silicone rubber tube, forming the cylindrical shape. This design employs silicone rubber which has an extremely small modulus (1–2 MPa) so that the constraint applied to the tested material is negligible. For temperature monitoring, a fine-wire thermal couple was embedded next to the fiber but far away from the Bragg grating section so that the inclusion effect was excluded.

The length of the specimen is also critical because the generalized plane strain condition is assumed in the derivation of governing equations. If the specimen is not sufficiently long, the strain field of the area where the Bragg gratings are located (in the middle of the specimen) can be affected by the free-edge effect. A supplementary numerical analysis was conducted to investigate the effect of the specimen length. The results indicated that the effect was

ignorable (less than 0.1%) when the specimen length was longer than 10 times of the gratings length. Since the length of the FBG employed in the experiment was 5 mm, the total length of both specimens was made to be 50 mm. The actual C-1 and C-2 configurations of the underfill material fabricated by the mold assembly are shown in Fig. 7(b).

An FBG data acquisition system consists of an FBG interrogation system (FBG-IS), an environmental chamber and a computer. The Bragg wavelength is measured by a commercial FBG interrogation system (Micron Optics sm125-500), which has a resolution of 1 pm and repeatability of 0.2 pm. The temperature is controlled by a computer-controlled oven (EC1A, Sun Systems).

Supplementary Experiment Using DSC

To determine the proper C-1 configurations, the curing kinetics of the polymer was measured using a differential scanning calorimeter (DSC). The heat flow was documented in the isothermal mode. The specimen was quickly ramped to 175°C and dwelled for several hours. The temperature profile and recorded heat flow curve of the material are shown in Fig. 8(a).

The total heat was obtained by integrating the area under the heat flow curve and it was 21.8*J*. The weight of the specimen was 0.0733*g* and the total exotherm, ΔH_{total}, was thus determined to be 330*J*/g. At arbitrary time *t*, the partial reaction heat was calculated by the partial integral of the area. The corresponding partial exotherm can be defined as $\Delta H(t)$. Then, the curing extent, $p(t)$, at time *t* can be simply determined as [54–59]

$$p(t) = \frac{\Delta H(t)}{\Delta H_{total}} \tag{39}$$

The evolution of curing extent determined from equation (39) is shown in Fig. 8(b). The *nth* order model (equation 28) was used to fit the measured curing extent, and the result is also shown in Fig. 8(b). The curing kinetics are determined to be k_c=0.0014/*s*.

Referring to Fig. 6(c), a specimen dimension of β=45 or smaller can be used for the C-1 configuration. Considering the practicality and commercial availability of silicone rubber tubing in the implementation, the inner diameter of the tube is 3/16" in specimen configuration C-1 and 3/32" in configuration C-2, which results in β_1=38 and β_2=19, respectively. It is to be noted that the curve of ΔH=400*J*/g k_c=0.0016/*s* in Fig. 6(c) is a conservative estimation and the final configurations assure uniform curing.

Evolution Properties

Before they were mounted on the mold, the FBGs were tested to obtain intrinsic properties. The bare FBGs were

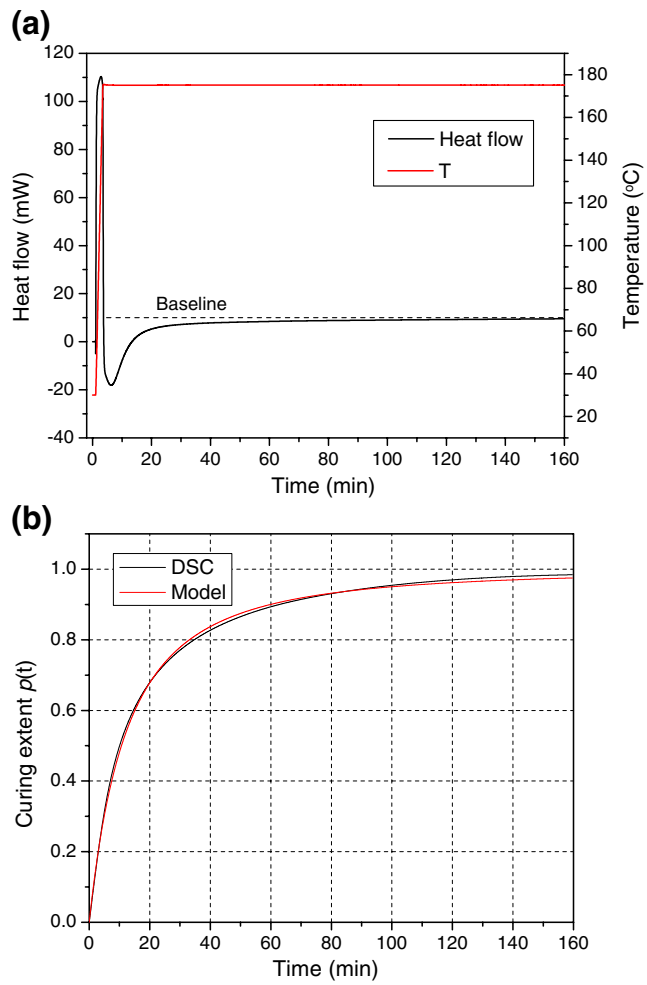

Fig. 8 (**a**) DSC raw data and (**b**) evolution of curing extent obtained from the DSC data

placed in the oven and the BW shift was documented as a function of temperature. Experimental results of two fibers used in C-1 and C-2 are shown in Fig. 9. The intrinsic BW shift is known to have a quadratic relationship with ΔT [60] and the results are:

$$\Delta\lambda_B^i\big|_{C-1} = 0.0126 \cdot (T-175) + 6.11 \cdot 10^{-6} \cdot (T-175)^2 \tag{40}$$

$$\Delta\lambda_B^i\big|_{C-2} = 0.0123 \cdot (T-175) + 6.74 \cdot 10^{-6} \cdot (T-175)^2 \tag{41}$$

where the reference temperature is 175°C.

After the FBG was aligned in the mold, the underfill material was injected into the silicone rubber tube. The specimen was then heated to 175°C at a ramp rate of 20°C/min and dwelled for 3.5 h. The evolution of BW throughout the entire process was recorded in both C-1 and C-2. The measured BW evolutions are shown in Fig. 10.

The BW shifts after the apparent gelation point in both configurations are plotted in Fig. 11. An offset is made on the time axis so that the time at the apparent gelation point

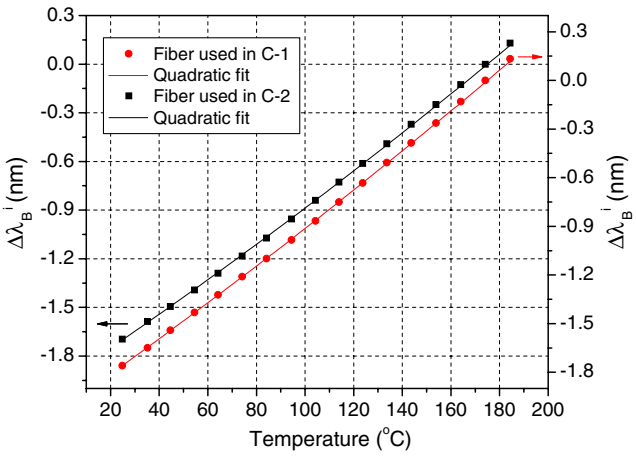

Fig. 9 Calibration results of FBGs used in two specimen configurations

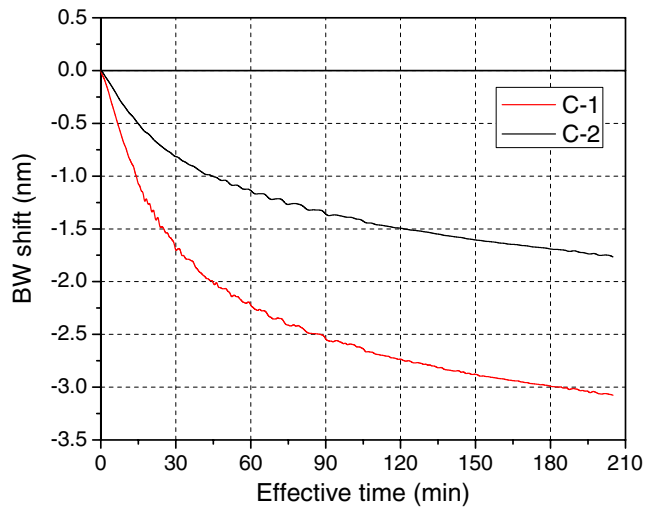

Fig. 11 BW shift after the apparent gelation point

is zero. When the curing is completed, the magnitude of $\Delta\lambda_B^d$ in C-1 is approximately two times larger than that in C-2, as expected from the larger volume stiffness in C-1.

Following the numerical procedures described in "Calculation of Evolution Properties," the evolutions of effective chemical shrinkage and modulus were calculated from the data in Fig. 11. The results are shown in Fig. 12(a) and (b), respectively. The effective chemical shrinkage accumulates much faster at the early stage of the polymerization, and gradually converges as the polymerization proceeds. The result indicates an expected gradual decrease in the polymerization speed.

Verification

Two tests are conducted to verify the validity of the proposed method: a self-consistency test to confirm the

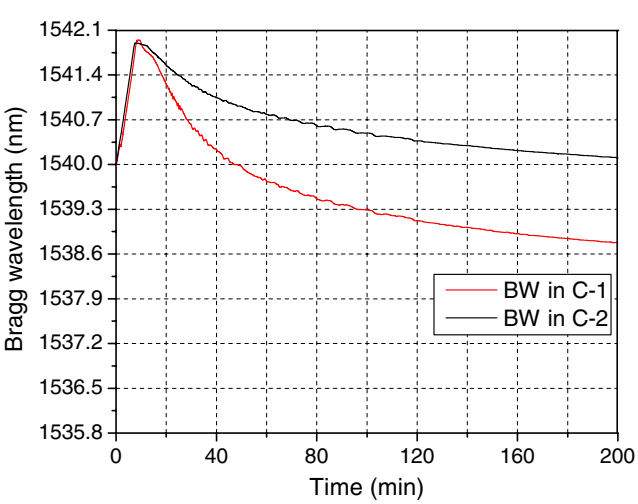

Fig. 10 Measured BW evolutions

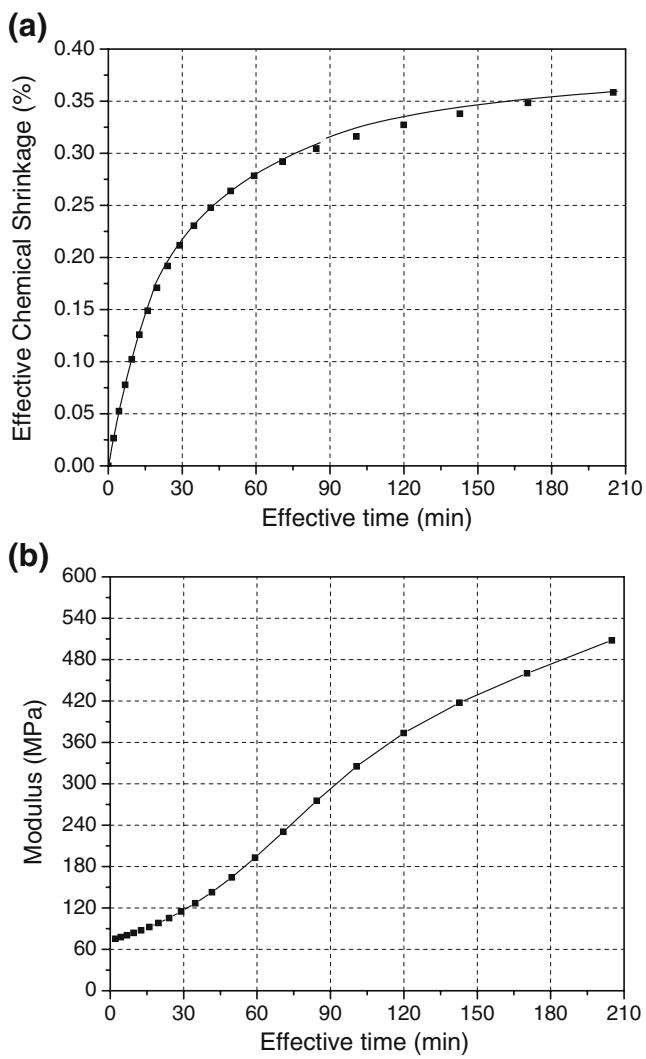

Fig. 12 Results of evolution properties: (**a**) effective chemical shrinkage and (**b**) modulus

accuracy of the raw data obtained from the two configurations, and a deformation measurement test to verify the validity of the evolution properties inversely calculated from the raw data.

Self-consistency Test

A different configuration was tested for the self-consistency of the measurements. The diameter of the polymer substrate was 1/8" which corresponds to a configuration of β=25 (denoted as C-3). The BW shift of the specimen during the curing process was measured experimentally. The experimental results of BW evolution are shown in Fig. 13(a).

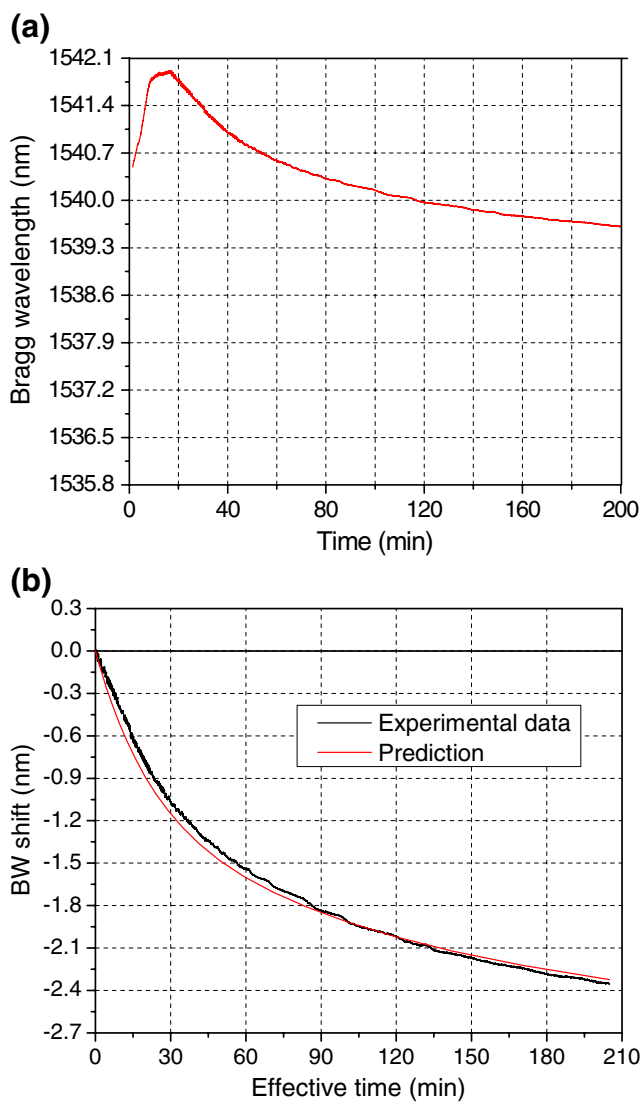

Fig. 13 (**a**) BW profile of the configuration C-3; the BW shift after the effective gelation point is compared with the predicted BW shift from the evolution data of Fig. 12 in (**b**)

The corresponding $\Delta\lambda_B^d$ after the apparent gelation point is plotted in Fig. 13(b). From the mathematical relationships described in "Mathematical Formulations," the BW shift of the specimen with a configuration of C-3 was calculated using the evolution properties of Fig. 12. The predicted results are compared with the experimental results Fig. 13(b). The two results agree well with each other, which confirms the accuracy of the raw data obtained from the proposed experimental procedure.

Warpage Prediction and Verification by using T/G Interferometry

The above self-consistency experiment verified that the results obtained from the proposed two specimen configurations can be used for prediction of the behavior of specimens in other configurations. However, it does not necessarily guarantee that the inversely determined evolution properties from the BW shift accurately represent the intrinsic properties of the material. The polymerization induced warpage of a bi-material strip was studied to further validate the accuracy of measured properties.

The bi-material strip used in the experiment is shown schematically in Fig. 14 (top figure). A high temperature tape was first wrapped around the edge of a rectangular glass strip. Then the polymer was poured to form a bi-material strip. The thickness of the glass strip and the polymer layer were 3.1 mm and 3.6 mm, respectively. The curing-induced warpage of the bottom surface was measured by Twyman/Green (T/G) interferometry during the entire curing process.

Twyman-Green (T/G) interferometry is a classical form of interferometry which involves the interference of coherent light [61]. A coherent light source, usually a laser, is collimated and then passed through a beam splitter where it is split into active and reference paths. The reference and active paths are reflected by the reference flat and the specimen, respectively. The reflected beams combine to interfere and create a fringe pattern seen by the observer, which represents the contour map of out-of-plane displacement (or warpage).

It should be noted that the specimen was installed in an oven for real-time observations during curing at the high curing temperature. The specimen holder inside the environmental chamber was designed specifically to accommodate the uncured bi-material strip, which required viewing from the bottom side. Figure 14 depicts the design that allows the required viewing direction. The specimen stage was designed to hold the uncured bi-material strip horizontally on top of a glass plate. Directly attached to the stage is a 45° mirror. This mirror reflects light both to and from the glass surface. A thin layer of aluminum was

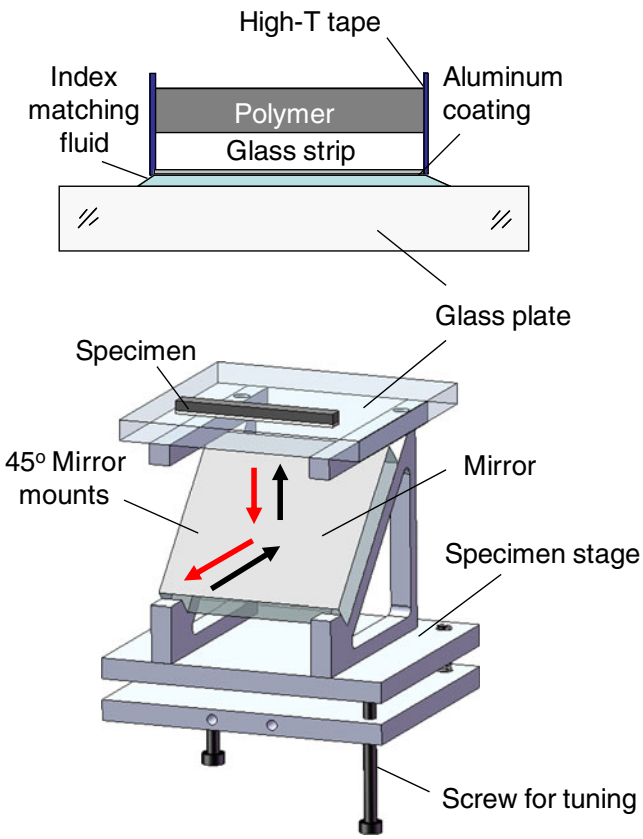

Fig. 14 Schematic drawing of bi-material joint (*top*) and specimen holder design for bottom viewing (*bottom*)

vacuum-deposited on the bottom surface of the glass strip. To eliminate the undesired fringes formed by the interference of the light reflected by the glass plate top surface and specimen surface, an index matching fluid was used to fill the gap between the bottom of the glass strip and the glass plate to avoid any undesired multiple reflections. With this configuration, the warpage of the bi-material, w, can be determined by [61]

$$w = \frac{N}{2n}\lambda \tag{42}$$

where n=1.5 which is the refractive index of the index matching fluid, N is the order of fringes, and λ is the wavelength of the laser.

Figure 15(a) shows the representative fringe patterns of the left half, obtained at various times during the curing process. An Argon laser with λ =514 nm was employed in the experiment, which produced a contour interval of 171.3 nm per fringe. The warpage as a function of the effective time is shown in Fig. 15(b).

The curing-induced warpage is also calculated numerically using the evolution properties. When a chemical shrinkage of $\Delta\varepsilon^{ch}$ occurs in the polymer layer

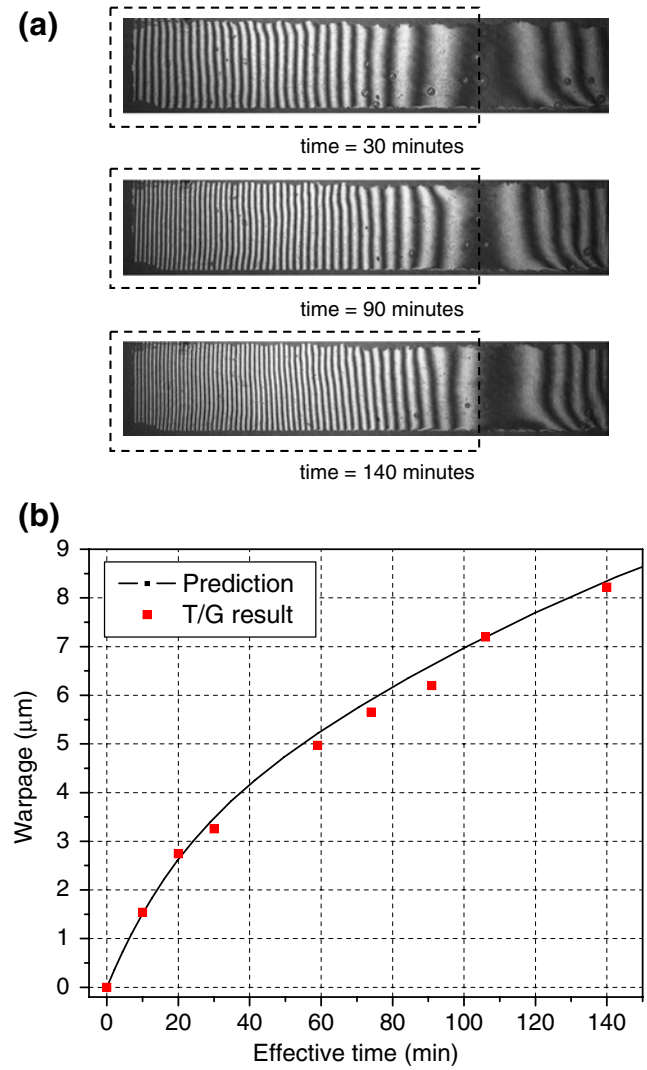

Fig. 15 **(a)** Representative fringe patterns of the left half of bi-material strip specimen at different effective time; the warpage obtained from the fringe patterns in **(a)** is compared with the predicted value in **(b)**

that has a thickness of t_1 and an instant modulus of E_1, the curing induced warpage of the glass substrate can be calculated by

$$\Delta w = \frac{3(t_1+t_2)E_1E_2t_1t_2L^2}{E_1^2t_1^4 + 6E_1E_2t_1^2t_2^2 + E_2^2t_2^4 + 4E_1E_2t_1^3t_2 + 4E_1E_2t_1t_2^3}\Delta\varepsilon^{ch} \tag{43}$$

where t_2 and E_2 are the modulus and the thickness of the glass strip, respectively, and L is the half length of the strip.

Since both effective chemical shrinkage and modulus evolve nonlinearly with time, the warpage change during each small time segment can be calculated first and the evolution of curing induced warpage can be then

determined by accumulating the warpage increments. The numerically predicted warpage evolution is also plotted in Fig. 15(b) for a comparison. The two results agree very well, which confirms the validity of the property measurement.

Discussions

The polymer modulus, E_s, was the only unknown parameter in the numerical procedure using equation (23). As can be seen from the explicit form of the nonlinear function F (from eqautions (16) to (21)), however, F is also a function of the Poisson's ratio of the polymer, ν_s, which can change as the polymer cures. As stated in our previous study [15], the effect of Poisson's ratio is negligible since the deformation of FBG is mainly induced by the axial stress of the polymer.

In order to quantify the effect of the Poisson's ratio, the values of F were calculated as a function of ν_s for polymers with a wide range of modulus (E_s=100 MPa, 500 MPa and 1GPa) and specimen configurations (β=20, 60 and 100). The results are plotted in Fig. 16, which confirms the negligible effect of Poisson's ratio (less than 1% change in F). In the implementation, a typical value of Poisson's ratio (say 0.3) can be used to define the function, F.

It should be noted that all the governing equations are based on the elasticity theory. However, polymeric materials in general exhibit some visco-elastic behavior. Stress relaxation can occur during curing progresses. Within the scope of linear visco-elasticity, the rates of relaxation would be identical in the two configurations since the modulus is stress-independent and only a function of the time [62, 63]. Consequently, the real-time modulus can be captured effectively in the two configurations. For the same reason, the effective chemical shrinkage can be overestimated if polymers show significant nonlinear visco-elastic behavior. Some form of compensation through a mathematical modeling may be needed for such polymers.

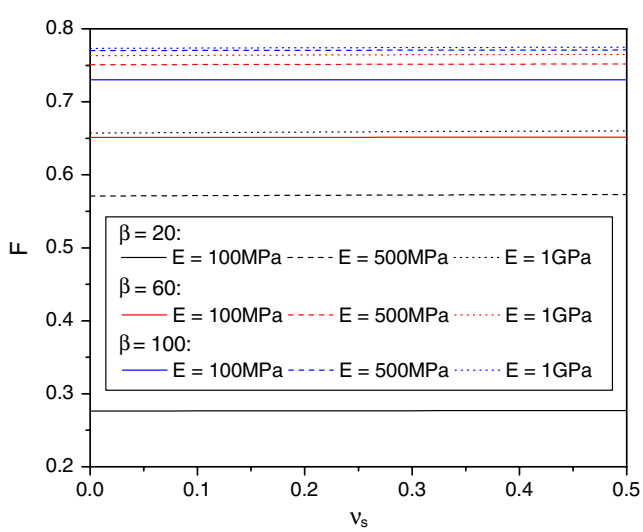

Fig. 16 Plot of F as a function of ν_s with various polymer modulus and specimen configurations

Conclusions

A novel measurement method utilizing embedded FBG sensors was proposed and implemented to simultaneously measure the effective chemical shrinkage and modulus evolutions of advanced polymers during the entire polymerization process. A theoretical basis and a numerical procedure were first established to determine inversely the evolution properties from the experimentally documented BW shifts of two specimen configurations. The numerical analyses were extended to provide general guidelines for selecting an optimum combination of the two specimen configurations. The proposed method was applied to a high-temperature curing thermosetting polymer using 20X and 40X configurations. The BW was documented after the effective gelation point, and the effective chemical shrinkage and modulus evolutions of the material during polymerization were determined successfully from the measured BW shifts.

Two independent tests were conducted to verify the validity of the proposed method. A self consistency test was performed using 25X and a deformation measurement test was conducted using a bi-material strip. The predicted results from the measured evolution properties were compared with the results of the verification tests. The two results agreed well with each other for both cases, which corroborated the accuracy and the validity of the proposed method.

References

1. Kelly G, Lyden C, Lawton W et al (1996) Importance of molding compound chemical shrinkage in the stress and warpage analysis of PQFP's. IEEE Trans Compon Packag Manuf Technol Part B, Adv Packag 19(2):296–300
2. Yang DG, Ernst LJ, van't Hof C et al () Vertical die crack stresses of Flip Chip induced in major package assembly processes. 1533-1538
3. Oota K, Saka M (2001) Cure shrinkage analysis of epoxy molding compound. Polym Eng Sci 41(2):1373–1379
4. Lu D, Wong CP (2009) Materials for advanced packaging. Springer-Verlag New York
5. Cook WD, Forrest M, Goodwin AA (1999) A simple method for the measurement of polymerization shrinkage in dental composites. Dent Mater 15(6):447–449

6. Hudson AJ, Martin SC, Hubert M et al (2002) Optical measurement of shrinkage in UV-cured adhesives. J Electron Packag 124(4):352–354
7. Li C, Potter K, Wisnom MR et al (2004) *In-situ* measurement of chemical shrinkage of MY750 epoxy resin by a novel gravimetric method. Compos Sci Technol 64(1):55–64
8. Russell JD (1993) Cure shrinkage of thermoset composites. Sample Quarterly 24(2):28–33
9. Snow AW, Armistead JP (1994) A simple dilatometer for thermoset cure shrinkage and thermal expansion measurements. J Appl Polym Sci 52(3):401–411
10. Thomas CL, Bur AJ (1999) *In-situ* monitoring of product shrinkage during injection molding using an optical sensor. Polym Eng Sci 39(9):1619–1627
11. Yu H, Mhaisalkar SG, Wong EH (2005) Cure shrinkage measurement of nonconductive adhesives by means of a thermo-mechanical analyzer. J Electron Mater 34(8):1177–1182
12. Spoelstra AB, Peters GWM, Meijer HEH (1996) Chemorheology of a highly filled epoxy compound. Polym Eng Sci 36(16):2153–2162
13. Zhang ZQ, Beatty E, Wong CP (2003) Study on the curing process and the gelation of epoxy/anhydride system for no-flow underfill for flip-chip applications. J Electron Mater 288 (4):365–371
14. Zhang ZQ, Yamashita T, Wong CP (2005) Study on the gelation of a no-flow underfill through Monte Carlo simulation. Macromol Mater Eng 206(8):869–877
15. Wang Y, Han B, Kim DW, Bar-Cohen A, Joseph P (2008) Integrated measurement technique for curing process-dependent mechanical properties of polymeric materials using fiber bragg grating. Exp Mech 48(1):107–117
16. Adolf D, Martin JE (1990) Time-cure superposition during cross-linking. Macromolecules 23(15):3700–3704
17. Eom Y, Boogh L, Michaud V et al (2000) Time-cure-temperature superposition for the prediction of instantaneous viscoelastic properties during cure. Polym Eng Sci 40(6):1281–1292
18. Lange J, Toll S, Manson JAE et al (1995) Residual stress build-up in thermoset films cured above their ultimate glass transition temperature. Polymer 36(16):3135–3141
19. Markovic S, Dunjic B, Zlatanic A et al (2001) Dynamic mechanical analysis study of the curing of phenol-formaldehyde novolac resins. J Appl Polym Sci 81(8):1902–1913
20. Sham ML, Kim JK (2005) Experiment and numerical analysis of the residual stresses in underfill resins for flip chip package applications. J Electron Packag 127(1):47–51
21. Stolov AA, Xie T, Penelle J et al (2000) Simultaneous measurement of polymerization kinetics and stress development in radiation-cured coatings: A new experimental approach and relationship between the degree of conversion and stress. Macromolecules 33(19):6970–6976
22. Gonzalez L, Ramis X, Salla JM et al (2007) Kinetic analysis by DSC of the cationic curing of mixtures of DGEBA and 6, 6-dimethyl (4, 8-dioxaspiro[2.5]octane-5, 7-dione). Thermochim Acta 464(1–2):35–41
23. Li WW, Liu F, Wei LH et al (2008) Curing behavior study of polydimethylsiloxane-modified allylated novolac/4, 4′-bismaleimidodiphenylmethane resin. J Appl Polym Sci 107(1):554–561
24. Luo ZH, Wei LH, Li WW et al (2008) Isothermal differential scanning calorimetry study of the cure kinetics of a novel aromatic maleimide with an acetylene terminal. J Appl Polym Sci 109 (1):525–529
25. Maji PK, Bhowmick AK (2009) Influence of number of functional groups of hyperbranched polyol on cure kinetics and physical properties of polyurethanes. J Polym Sci, A, Polym Chem 47(3):731–745
26. McGee SH (1982) Curing characteristics of particulate-filled thermosets. Polym Eng Sci 22(8):484–491
27. Zhang ZQ, Wong CP (2004) Modeling of the curing kinetics of no-flow underfill in flip-chip applications. IEEE Trans Compon Packag Technol 27(2):383–390
28. Bogetti TA, Gillespie JW (1992) Process-induced stress and deformation in thick-section thermoset composite laminates. J Compos Mater 26(5):626–660
29. Huang YJ, Liang CM (1996) Volume shrinkage characteristics in the cure of low-shrink unsaturated polyester resins. Polymer 37 (3):401–412
30. Adolf DB, Martin JE, Chambers RS et al (1998) Stresses during thermoset cure. J Mater Res 13(3):530–550
31. Kluppel M, Schuster RH (1997) Structure and properties of reinforcing fractal filler networks in elastomers. Rubber Chem Technol 70:243–255
32. Alonso MV, Oliet M, Garcia J et al (2006) Gelation and isoconversional kinetic analysis of lignin-phenol-formaldehyde resol resins cure. Chem Eng J 122(3):159–166
33. O'Brien DJ, White SR (2003) Cure kinetics, gelation, and glass transition of a bisphenol F epoxide. Polym Eng Sci 43(4):863–874
34. Yu H, Mhaisalkar SG, Wong EH (2005) Observations of gelation and vitrification of a thermosetting resin during the evolution of polymerization shrinkage. Macromol Rapid Commun 26 (18):1483–1487
35. Yu H, Mhaisalkar SG, Wong EH et al (2006) Time-temperature transformation (TTT) cure diagram of a fast cure non-conductive adhesive. Thin Solid Films 504:331–335
36. Chen KM, Jiang DS, Kao NH et al (2006) Effects of underfill materials on the reliability of low-K flip-chip packaging. Microelectron Reliab 46(1):155–163
37. Lange J, Toll S, Manson JAE et al (1997) Residual stress build-up in thermoset films cured below their ultimate glass transition temperature. Polymer 38(4):809–815
38. Meuwissen MHH, de Boer HA, Steijvers H et al (2006) Prediction of mechanical stresses induced by flip-chip underfill encapsulants during cure. Int J adhes Adhes 26(4):212–225
39. Yang DG, Jansen KMB, Ernst LJ et al. (2004) Prediction of process-induced warpage of IC packages encapsulated with thermosetting polymers. *Electronic Components and Technology Conference*, pp. 98–105
40. Yu H, Mhaisalkar SG, Wong EH et al (2004) Evolution of Mechanical Properties and Cure Stresses in Non-Conductive Adhesives Used for Flip Chip Interconnects. *Electronic Packaging Technology Conference*, pp. 468–472
41. Aggelopoulos A, Karalekas D (2001) Determination of cure shrinkage in SL layer built plates using lamination theory. Adv Compos Lett 10(1):7–12
42. Attin T, Buchalla W, Kielbassa AM et al (1995) Curing shrinkage and volumetric changes of resin-modified glass ionomer restorative materials. Dent Mater 11(5–6):359–362
43. Braga RR, Ferracane JL (2002) Contraction stress related to degree of conversion and reaction kinetics. J Dent Res 81 (2):114–118
44. Fano V, Ortalli I, Pizzi S et al (1997) Polymerization shrinkage of microfilled composites determined by laser beam scanning. Biomaterials 18:467–470
45. Ishida H, Low HY (1997) A study on the volumetric expansion of benzoxazine-based phenolic resin. Macromolecules 30 (4):1099–1106
46. Park SH, Krejci I, Lutz F (1999) Consistency in the amount of linear polymerization shrinkage in syringe-type composites. Dent Mater 15(6):442–446
47. Watts DC, Cash AJ (1991) Determination of polymerization shrinkage kinetics in visible-light-cured materials—methods development. Dent Mater 7(4):281–287
48. Hocker GB (1979) Fiberoptic sensing of pressure and temperature. Appl Opt 18(9):1445–1448

49. Gafsi R, El-Sherif MA (2000) Analysis of induced-birefringence effects on fiber Bragg gratings, Opt Fiber Technol 6(3):299–323
50. Zhang Y, Feng DJ, Liu ZG et al (2001) High-sensitivity pressure sensor using a shielded polymer-coated fiber Bragg grating. IEEE Photonics Technol Lett 13(6):618–619
51. Rabil CD, Harrington JA (1999) Mechanical properties of hollow glass waveguides. Opt Eng 38(9):1490–1499
52. Tao XM, Tang LQ, Du WC et al (2000) Internal strain measurement by fiber Bragg grating sensors in textile composites. Compos Sci Technol 60(5):657–669
53. Lopez-Higuera JM (2002) Handbook of optical fibre sensing technology. Wiley, England
54. Cai HY, Li P, Sui G et al (2008) Curing kinetics study of epoxy resin/flexible amine toughness systems by dynamic and isothermal DSC. Thermochim Acta 473(1–2):101–105
55. Costa ML, Botelho EC, Rezende MC (2006) Monitoring of cure kinetic prepreg and cure cycle modeling. J Mater Sci 41 (13):4349–4356
56. Fernandez-Francos X, Salla JM, Mantecon A et al (2008) Crosslinking of mixtures of DGEBA with 1, 6-dioxaspiro[4, 4] nonan-2, 7-dione initiated by tertiary amines. I. Study of the reaction and kinetic analysis. J Appl Polym Sci 109(4):2304–2315
57. Han SJ, Wang KK (1997) Analysis of the flow of encapsulant during underfill encapsulation of flip-chips. IEEE Trans Compon Packag Manuf Technol Part B, Adv Packag 20(4):424–433
58. He Y (2005) Chemical and diffusion-controlled curing kinetics of an underfill material. Microelectron Reliab 45(3–4):689–695
59. Omrani A, Simon LC, Rostami AA et al (2008) Cure kinetics, dynamic mechanical and morphological properties of epoxy resin-IM6NiBr2 system. Eur Polym J 44(3):769–779
60. Kim KJ, Bar-Cohen A, Han B (2007) Thermo-optical modeling of polymer fiber Bragg grating illuminated by light emitting diode. Int J Heat Mass Transfer 50(25–26):5241–5248
61. Post D, Han B, Ifju P (1994) High sensitivity Moire. Springer-Verlag New York
62. Goertzen WK, Kessler MR (2006) Creep behavior of carbon fiber/epoxy matrix composites. Mater Sci Eng, A 421:217–225
63. Yang J, Zhang Z, Schlarb AK, Friedrich K (2006) On the characterization of tensile creep resistance of polyamide 66 nanocomposites. Part I. Experimental results and general discussions. Polymer 47:2791–2801